Draft version May 10, 2010
Preprint typeset using LaTeX style emulateapj v. 11/10/09

USING RADIO HALOS AND MINIHALOS TO MEASURE THE DISTRIBUTIONS OF MAGNETIC FIELDS AND COSMIC-RAYS IN GALAXY CLUSTERS

Uri Keshet[1] and Abraham Loeb
Harvard-Smithsonian Center for Astrophysics, 60 Garden St., Cambridge, MA 02138, USA
Draft version May 10, 2010

ABSTRACT

Some galaxy clusters show diffuse radio emission in the form of giant halos (GHs) on Mpc scales or minihalos (MHs) on smaller scales. Comparing VLA and XMM radial profiles of several such clusters, we find a universal linear correlation between radio and X-ray brightness, and show that the radio emissivity scales as $j_\nu \propto n^2 T^\kappa$ within each cluster, where n and T are the local electron number density and temperature, and $\kappa \lesssim 1$. We argue that the tight correlation and this scaling, combined with morphological and spectral evidence, indicate that both GHs and MHs arise from secondary electrons and positrons, produced in cosmic-ray ion (CRI) collisions with the strongly magnetized ($B \gtrsim 3$ μG) intracluster gas. When the magnetic energy density drops below that of the microwave background, the radio emission weakens considerably, producing halos with a clumpy morphology (*e.g.,* RXC J2003.5-2323 and A2255) or a distinct radial break. We thus measure a magnetic field $B = 3$ μG at a radius $r \simeq 110$ kpc in A2029 and at $r \simeq 50$ kpc in Perseus. The spectrum of secondaries, produced from hadronic collisions of ~ 20 GeV CRI, reflects the energy dependence of the collision cross section. We use the observed spectra of halos, in particular where they steepen with increasing radius or frequency, to *(i)* measure $B \simeq 10(\nu/700\ \mathrm{MHz})$ μG, with ν the spectral break frequency; *(ii)* identify a correlation between the average spectrum and the central magnetic field; and *(iii)* infer a CRI spectral index $s \lesssim -2.7$ and energy fraction $\xi_p \sim 10^{-3.6\pm0.2}$ at particle energies above 10 GeV. Our results favor a model where CRI diffuse away from their sources (which are probably supernovae, according to a preliminary correlation with star formation), whereas the magnetic fields are generated by mergers in GHs and by core sloshing in MHs.

Subject headings: galaxies: clusters: general — intergalactic medium — X-rays: galaxies: clusters — radio continuum: general — magnetic fields

1. INTRODUCTION

Giant halos (GHs) appear as diffuse radio emission on $\sim$ Mpc scales in merging galaxy clusters (for a review, see Feretti & Giovannini 2008). GHs were identified in about a quarter of all clusters with X-ray luminosities $L_X > 5 \times 10^{44}$ erg s^{-1} at redshifts $0.2 < z < 0.4$ (Brunetti et al. 2007). L_X and the specific radio power P_ν of GH clusters are tightly correlated. The GH distribution in clusters is bimodal, with most clusters showing no associated GH at a sensitivity threshold ~ 10 times better than the signal expected from the L_X–P_ν correlation (Brunetti et al. 2007). Recently, Kushnir et al. (2009, henceforth K09) made the important observation that these properties are reproduced if GHs are synchrotron emission from secondary cosmic ray electrons and positrons (CRE) produced in *p*-*p* cosmic ray proton (CRP) collisions, gyrating in strong magnetic fields B that saturate $P_\nu(B)$ by rendering Compton losses negligible. Other models, notably turbulent reacceleration of electrons (for a review see Petrosian & Bykov 2008), do not naturally produce the correlation and bimodality that are observed[2].

Radio minihalos (MHs) are found in cool core clusters (CCs). They extend roughly over the cooling region (Gitti et al. 2002), encompassing up to a few percent of the typical GH volume. Detecting MHs is more challenging than GHs, due to their smaller size and proximity to an active galactic nucleus (AGN), so only few MHs have been well studied. A morphological association between MH edges and cold fronts (CFs; Mazzotta & Giacintucci 2008) suggests a link between MHs and sloshing activity in the core. Such CFs are found in about half the CCs, and are probably present in many more (Markevitch & Vikhlinin 2007). They are thought to be tangential discontinuities that isolate regions magnetized by bulk shear flow at smaller radii (also referred to as below, or inside the CF; Keshet et al. 2009).

Both GHs and MHs are usually characterized by a regular morphology, low surface brightness, little or no polarization, and spectral indices $\alpha_\nu \equiv d\log(P_\nu)/d\log\nu \simeq -(1.0-1.5)$, with ν the frequency. However, a few GHs have a clumpy or filamentary morphology, such as in RXC J2003.5-2323 (Giacintucci et al. 2009), A2255, and A2319 (Murgia et al. 2009, henceforth M09). Strong polarization was so far detected in one GH (at a 20%–40% level, in A2255; see Govoni et al. (2005); weaker polarization, $2-7\%$ on average, was found in MACS J0717.5 +3745; see Bonafede et al. (2009)), and in one MH (at a $10\%-20\%$ level, in A2390; Bacchi et al. 2003). Spectral steepening with increasing r, increasing ν, or decreasing T, has been reported in several radio halos (Feretti & Giovannini 2008; Ferrari et al. 2008; Giovannini et al. 2009, and references therein); typically, α steepens from -1.0 to $-(1.3$–$1.5)$ in uncontaminated regions (see §5.2). A handful of GHs show a steep, $\alpha < -1.5$ spectrum, such

[1] Einstein fellow
[2] In the sense that the small dispersion above $P_\nu(L_X)$ is not reproduced, and many assumptions (*e.g.,* Brunetti & Lazarian 2007) are needed. For a different opinion, see Brunetti et al. (2009).

as in A521 ($\alpha = -1.86 \pm 0.08$; Dallacasa et al. 2009) and in A697 ($\alpha = -(1.7$–$1.8)$; Macario et al. 2010).

In §2 we show that GHs and MHs follow the same correlation between radio emission and *coincident* X-ray luminosity. A tight correlation between the radio and X-ray brightness is presented in §3, and is used to derive the scaling of radio emissivity with the local electron number density n and temperature T. We then show in §4 that the inferred scaling favors a model in which the radio emission in both GHs and MHs originates from secondary CRE produced by collisions of cosmic-ray ions (CRI) with the intracluster gas, synchrotron radiating most of their energy in strong magnetic fields, as proposed by K09 for GHs. We study the morphological and spectral properties of the halos in §5, presenting new methods for measuring the distributions of CRI and magnetic fields. Finally, we discuss the origin of the CRI and magnetic fields in §6, and summarize our results. We assume a Hubble constant $H = 70$ km s^{-1} Mpc^{-1}. Error bars are 1σ confidence intervals.

2. GHS AND MHS: SIMILAR CORRELATION BETWEEN RADIO AND COINCIDENT X-RAY EMISSION

The 19 X-ray bright GH clusters in the Brunetti et al. (2007) sample follow the correlation

$$(\nu P_{\nu,1.4})_{45} \simeq 10^{-4.2\pm0.3} L^{1.7}_{X[0.1,2.4],45} \ , \qquad (1)$$

where the subscript 45 denotes units of 10^{45} erg s^{-1}. Here, $X[\epsilon_1, \epsilon_2]$ designates integration over photon energies between ϵ_1 and ϵ_2 measured in keV (we use $[0.1, 2.4]$ unless otherwise stated), and subscript 1.4 means that the radio signal is evaluated at a frequency $\nu = 1.4$ GHz. The normalization uncertainty in Eq. (1) is dominated by an intrinsic scatter among halos, needed to obtain an acceptable fit (chosen as $\chi^2/N = 1$ with N being the number of degrees of freedom). Accounting for dispersion in P_ν leads to the correlation Eq. (1), in agreement with K09, somewhat flatter than in Cassano et al. (2006).

A sample of 6 well-studied MHs had been reported (Cassano et al. 2008) as being "barely" consistent with the GH correlation of Cassano et al. (2006). However, we find that this sample agrees well with Eq. (1) with $\chi^2/N = 1.4$. Nevertheless, within a partly overlapping sample of 6 MHs studied recently (Govoni et al. 2009, M09), the MHs appear significantly underluminous with respect to the prediction of Eq. (1) after a careful removal (M09) of the contamination from AGN.

These results do not imply that MHs are intrinsically fainter than GHs. Rather, MHs have comparable radio power, if one corrects for their smaller size. A natural generalization of Eq. (1) applicable for both GHs and MHs would replace L_X with the luminosity of the radio bright region, $\bar{L}_X$. Following M09, we define the radio bright region based on the surface brightness condition $I_\nu(r)/I_\nu(r=0) > e^{-3} \simeq 5\%$, with r being the radial distance from the cluster center; equivalently, the radius of this region is $R_\nu = 3r_e$, with r_e the e-fold radius.

A quick way to estimate $\bar{L}_X$ is to correct L_X using a model for the X-ray brightness profile of the cluster. Using an isothermal β-model (Cavaliere & Fusco-Femiano 1976), we find that

$$\bar{L}_X = L_X \frac{\left(1 + R_\nu^2/r_c^2\right)^{\frac{3}{2}-3\beta} - 1}{\left(1 + R_X^2/r_c^2\right)^{\frac{3}{2}-3\beta} - 1} \ . \qquad (2)$$

We use individual cluster β-model parameters r_c and β from the literature; see Table 1 for details. The radius R_X of the X-ray region considered must be finite in order to ensure convergence. Its choice is somewhat arbitrary; we use $R_X = 12 r_c$ so $R_\nu < R_X$ for all halos in the M09 sample.

Figure 1 shows various GHs and MHs in the resulting $\bar{L}_X - \nu P_\nu$ plane. Replacing L_X by $\bar{L}_X$ results in slightly better agreement of the M09 GHs with Eq. (1), yielding $\chi^2/N = 1.3$ instead of 1.6 (before propagating β model uncertainties). However, the MH agreement becomes much better, $\chi^2/N = 2.4$ instead of 3.7. Note that the fit is not expected to be as good for MHs as it is for GHs, because a β-model is less appropriate for a CC. These results suggest that the relation between radio and X-ray emission is similar in GHs and in MHs. For more accurate, model-independent results, we next consider the radio and X-ray morphologies.

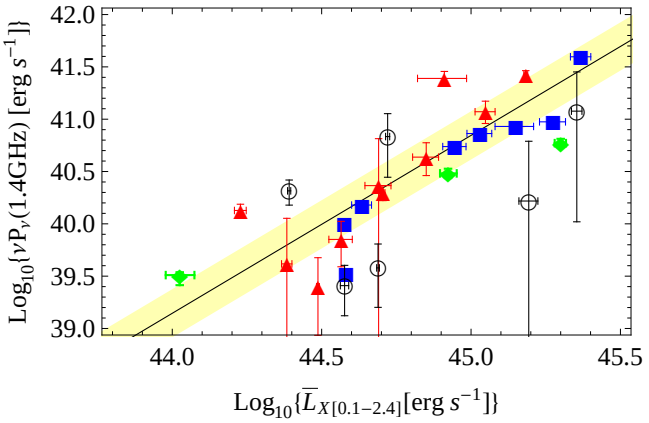

FIG. 1.— The 1.4 GHz radio power νP_ν of GHs (red triangles) and MHs (black circles) from M09, plotted against the 0.1-2.4 keV X-ray luminosity $\bar{L}_X$ of the radio bright region (see §2 and table 1 for details). The total X-ray luminosity L_X is used in cases where $\bar{L}_X$ could not be determined, for GHs (blue squares, from Cassano et al. 2006) and MHs (green diamonds, from Cassano et al. 2008). The solid line and shaded region show the best fit and 1σ interval of the GH correlation in Eq. (1).

3. RADIO-X-RAY BRIGHTNESS CORRELATION AND THE IMPLIED RADIO EMISSIVITY $j_\nu \sim n^2 T^\kappa$

A more useful manifestation of the radio-X-ray correlation is the morphological similarity between radio and X-ray emission. A linear correlation between the radio surface brightness I_ν and the X-ray brightness F_X was found in some GHs (Govoni et al. 2001a). Figure 2 shows the radial profile of the dimensionless ratio η between radio and X-ray brightness, for all 5 GHs and 4 MHs with published radial profiles from both VLA (M09) and XMM (Snowden et al. 2008) observations. We normalize η by the local temperature $T_{10} = (k_B T/10$ keV) (motivated by the discussion below), where k_B is Boltzmann's constant, and use r_{500}, the radius enclosing 500 times

TABLE 1
PARAMETERS OF HALO CLUSTERS IN THE SAMPLE

(1) Cluster	(2) Type	(3) z	(4) $L_{X[0.1-2.4]}$	(5) T	(6) r_e	(7) $\langle j \rangle$	(8) β	(9) r_c	(10) $\bar{L}_{X[0.1-2.4]}$	(11) $B_{0,min}$	(12) $\langle \alpha \rangle$	(13) $Z(0.1r_{500})$
A401	GH	0.074	$6.3^{+0.1}_{-0.1}$ (R02)	$7.8^{+0.2}_{-0.2}$ (A09a)	109^{+21}_{-15}	$4.1^{+1.3}_{-1.0}$	$0.61^{+0.01}_{-0.01}$ (C07)	$175^{+7.9}_{-7.1}$	$3.1^{+0.1}_{-0.1}$	7.4	$\alpha^{1.4}_{0.6} = -1.4$ (R81)	—
A545	GH	0.154	$5.7^{+0.5}_{-0.5}$ (C06)	$5.5^{+6.2}_{-2.1}$ (D93)	150^{+11}_{-11}	$12.0^{+2.2}_{-1.9}$	—	—	—	—	$\alpha_{1.4} < -1.4$ (G03)	—
A665	GH	0.182	$9.8^{+1.0}_{-1.0}$ (C06)	$7.9^{+0.2}_{-0.2}$ (A09a)	236^{+18}_{-15}	$7.0^{+1.0}_{-1.0}$	$0.54^{+0.01}_{-0.01}$ (B06)	$139^{+4.2}_{-4.2}$	$7.1^{+1.0}_{-1.0}$	16.8	$\alpha^{1.4}_{0.3} = -1.04^{0.02}_{-0.02}$ (F04b)	0.30 ± 0.06
A773	GH	0.217	$6.1^{+0.5}_{-0.5}$ (B00)	$7.4^{+0.3}_{-0.3}$ (A09a)	111^{+10}_{-10}	$11.0^{+2.4}_{-2.0}$	$0.61^{+0.01}_{-0.01}$ (B06)	$131^{+4.2}_{-4.2}$	$3.7^{+0.5}_{-0.5}$	12.0	$\alpha^{1.4}_{0.3} = -1.02^{+0.26}_{-0.26}$ (K01)	0.41 ± 0.16
A2163	GH	0.203	$17.1^{+0.3}_{-0.3}$ (R02)	$14.7^{+0.3}_{-0.3}$ (V09)	394^{+7}_{-7}	$9.2^{+0.4}_{-0.4}$	$0.80^{+0.03}_{-0.03}$ (C07)	$371^{+21.4}_{-20.7}$	$15.2^{+0.3}_{-0.3}$	19.6	$\alpha^{1.4}_{0.07} = -1.02$ (V09)	0.25 ± 0.07
A2218	GH	0.176	$4.6^{+0.2}_{-0.2}$ (E98)	$7.2^{+0.2}_{-0.2}$ (A09a)	76^{+26}_{-18}	$20.0^{+14.0}_{-9.0}$	$0.77^{+0.01}_{-0.01}$ (B06)	$190^{+4.6}_{-4.3}$	$2.4^{+0.2}_{-0.2}$	7.4	$\alpha^{1.4}_{0.3} = -1.46^{1.0}_{-1.0}$ (K01)	0.37 ± 0.15
A2219	GH	0.226	$12.7^{+1.0}_{-1.0}$ (C06)	$9.5^{+0.6}_{-0.4}$ (C06)	359^{+18}_{-14}	$5.4^{+0.6}_{-0.6}$	$0.66^{+0.07}_{-0.01}$ (F04)	$208^{+99.1}_{-23.8}$	$11.2^{+1.0}_{-1.0}$	24.9	$\alpha^{1.4}_{0.3} = -0.9^{+0.1}_{-0.1}$ (O07)	—
A2254	GH	0.178	$4.3^{+0.4}_{-0.4}$ (B00)	$7.5^{+0.5}_{-1.5}$ (C06)	238^{+57}_{-39}	$9.7^{+3.4}_{-2.8}$	—	—	—	—	$\alpha^{1.7}_{1.4} \sim -1.2$ (G01)	—
A2255	GH	0.081	$2.6^{+0.1}_{-0.1}$ (C06)	$6.9^{+0.1}_{-0.1}$ (A09a)	203^{+6}_{-6}	$3.4^{+0.2}_{-0.2}$	$0.80^{+0.03}_{-0.03}$ (C07)	$424^{+25.0}_{-22.9}$	$1.7^{+0.1}_{-0.1}$	7.3	$\alpha^{1.4}_{0.3} = -2.06^{+0.57}_{-0.57}$ (K01)	—
A2319	GH	0.056	$8.2^{+0.1}_{-0.1}$ (C07)	$8.8^{+0.3}_{-0.2}$ (C06)	198^{+7}_{-6}	$5.4^{+0.4}_{-0.4}$	$0.59^{+0.01}_{-0.01}$ (C07)	$203^{+10.0}_{-9.3}$	$5.1^{+0.1}_{-0.1}$	9.7	$\alpha^{1.4}_{0.3} = -1.28^{+0.35}_{-0.35}$ (K01)	0.31 ± 0.04
A2744	GH	0.308	$13.1^{+2.4}_{-2.4}$ (C06)	$8.6^{+0.4}_{-0.3}$ (C06)	275^{+9}_{-9}	$25.0^{+1.7}_{-1.6}$	$0.57^{+0.12}_{-0.06}$ (F04)	$251^{+120}_{-2.4}$	$8.1^{+2.4}_{-2.4}$	15.7	$\alpha^{1.4}_{0.07} = -1.1$ (V09)	—
RXJ1314	GH	0.244	$7.3^{+0.7}_{-0.7}$ (M01)	$8.7^{+0.4}_{-0.4}$ (M01)	160^{+61}_{-38}	$12.0^{+8.0}_{-5.0}$	$0.77^{+0.23}_{-0.23}$ (V02)	286^{+100}_{-100}	$4.9^{+0.7}_{-0.7}$	10.7	$\alpha^{1.4}_{0.07} = -1.4$ (V09)	—
A1835	MH	0.253	$16.3^{+1.2}_{-1.2}$ (B00)	$7.1^{+0.1}_{-0.1}$ (A09a)	102^{+70}_{-31}	$33.0^{+22.0}_{-13.0}$	$0.53^{+0.00}_{0.00}$ (S08)	$29.0^{+0.3}_{-0.3}$	$15.6^{+1.2}_{-1.2}$	32.6	—	0.28 ± 0.05
A2029	MH	0.076	$8.5^{+0.1}_{-0.1}$ (C07)	$6.9^{+0.1}_{-0.1}$ (A09a)	53^{+6}_{-6}	$54.0^{+19.0}_{-13.0}$	$0.58^{+0.00}_{0.00}$ (C07)	$59.3^{+1.4}_{-1.4}$	$4.9^{+0.1}_{-0.1}$	9.3	$\alpha_{0.2} \simeq -1.35$ (S83)	0.38 ± 0.06
A2390	MH	0.228	$15.8^{+0.2}_{-0.2}$ (A03)	$9.3^{+0.1}_{-0.1}$ (B07)	36^{+4}_{-4}	3100^{+1000}_{-800}	$0.47^{+0.00}_{0.00}$ (S08)	$46.0^{+1.0}_{-1.0}$	$5.3^{+0.2}_{-0.2}$	9.4	$\alpha^{0.4}_{0.07} \simeq -1.10$ (A06)	—
Ophiuchus	MH	0.028	$6.1^{+0.2}_{-0.2}$ (C07)	$10.2^{+0.3}_{-0.4}$ (C07)	105^{+13}_{-11}	$4.7^{+0.9}_{-0.8}$	$0.75^{+0.04}_{-0.03}$ (C07)	$199^{+16.4}_{-15.0}$	$3.8^{+0.2}_{-0.2}$	6.8	—	—
Perseus	MH	0.018	$8.2^{+0.1}_{-0.1}$ (C07)	$6.4^{+0.1}_{-0.1}$ (F04)	23^{+1}_{-1}	3600^{+500}_{-500}	$0.54^{+0.01}_{0.00}$ (C07)	$45.0^{+1.4}_{-0.7}$	$2.5^{+0.1}_{-0.1}$	5.4	$\alpha^{1.5}_{0.3} \sim -1.2$ (G04)	0.42 ± 0.01
RXJ1347	MH	0.451	$27.5^{+1.1}_{-1.1}$ (F04)	$10.7^{+0.1}_{-0.1}$ (A09b)	52^{+17}_{-11}	1800^{+700}_{-500}	$0.54^{+0.00}_{0.00}$ (B06)	$23.3^{+0.5}_{-0.5}$	$22.6^{+1.1}_{-1.1}$	31.9	—	0.39 ± 0.04

Columns: (1) cluster name (1RXS J131423 .6-251521 abbreviated RXJ1314; RXJ1347.5-1145 abbrev. RXJ1347); (2) halo type (GH or MH); (3) redshift z; (4) X-ray luminosity between 0.1 and 2.4 keV, in units of 10^{44} erg s^{-1}; (5) temperature in keV; (6) e-fold radius of radio brightness in kpc (M09); (7) average 1.4 GHz specific emissivity in units of 10^{-43} erg s^{-1} cm^{-3} Hz^{-1} (M09); (8-9) exponent β and core radius r_c in kpc for an isothermal β-model of the cluster; (10) X-ray luminosity of the radio bright region (see §2) between 0.1 and 2.4 keV, in units of 10^{44} erg s^{-1}; (11) minimal central magnetic field $B_{0,min}$ in units of μG, assuming the β-model and that $B(r = 3r_e) = B_{cmb}$ ($f_{ic} = 0.5$ in Eq. 9); (12) average spectral index $\alpha^{\nu_2}_{\nu_1}$ between frequencies (in GHz) ν_1 and ν_2, or α_ν around frequency ν; (13) Metallicity measured at $r = 0.1r_{500}$ in solar units (Snowden et al. 2008).

References: References are given in parentheses. For conflicting references, we adopt the tighter estimate if applicable, and otherwise use the most resent result. A03: Allen et al. (2003); A06: Augusto et al. (2006); A09a: Andersson et al. (2009); A09b: Anderson et al. (2009); B00: Böhringer et al. (2000); B03: Bacchi et al. (2003); B06: Bonamente et al. (2006); B07: Baldi et al. (2007); C06: Cassano et al. (2006); C07: Chen et al. (2007); D93: David et al. (1993); F04: Fukazawa et al. (2004); F04b: Feretti et al. (2004a) F07: Feretti et al. (1997); G01: Govoni et al. (2001b); G03: Giovannini et al. (2003); G04: Gitti et al. (2004); H80: Harris et al. (1980); K01: Kempner & Sarazin (2001); M01: Matsumoto et al. (2001); M00: Matsumoto et al. (2000); M07: Morandi et al. (2007); R81: Roland et al. (1981) R02: Reiprich & Böhringer (2002); S83: Slee & Siegman (1983); S08: Santos et al. (2008); S09: Sanderson et al. (2009); V02: Valtchanov et al. (2002); V09: van Weeren et al. (2009); WB03: Worrall & Birkinshaw (2003); W00: White (2000).

the critical density of the Universe (calculated using the best fit of Zhang et al. 2008).

All halos except the MH in Perseus (A426) converge on a similar value of η at small radii. The innermost GH data is best fit by

$$\eta \equiv \frac{\nu I_\nu(1.4\ \mathrm{GHz})}{T_{10} F_{X[0.1-2.4]}} = 10^{-4.3\pm0.2}\ , \qquad (3)$$

where the uncertainty is again larger than the measurement errors and mostly attributed to intrinsic scatter between halos (dominated here by the radio bright GH in A665). The MHs too lie within this 1σ scatter, except Perseus which is significantly (3.6σ) brighter in radio. Therefore, Eq. (3) appears to hold at small radii for both GHs and MHs. The special case of Perseus and the relatively high radio brightness of A665 are discussed in §6.2. As in §2, we used only GHs, which are better understood than MHs, to derive the correlation Eq. (3). If, instead, we use the innermost data of both GHs and MHs, the best fit becomes $\eta \simeq 10^{-4.2\pm0.4}$, a slightly higher value and broader distribution than in Eq. (3), mainly due to the bright MH in Perseus.

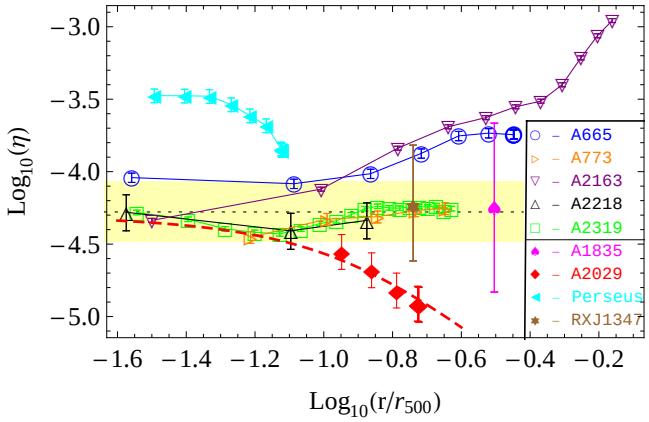

FIG. 2.— Radial profiles of the radio-to-X-ray ratio η (defined in Eq. (3)) in the GHs (open symbols) and MHs (filled symbols) with overlapping profiles from VLA (M09) and from XMM (Snowden et al. 2008, k-corrected). The MH data is shown only in regions where the AGN contamination is $< 10\%$. Error bars are the 1σ confidence intervals of the radio normalization I_0 (M09), and the solid lines serve to guide the eye. The 1σ best fit of Eq. (3) is shown as a thin dashed line in a shaded region. Our best fit model for A2029 (dashed; see §5.1) is also shown.

Although there is some scatter among different halos, η appears to be fairly uniform within a given cluster at small radii and in uncontaminated regions, as seen in Fig. 2. The monotonically rising $\eta(r)$ profiles in A665 and A2163 are probably associated with merger shocks, which were discovered in both clusters (Markevitch & Vikhlinin 2001), and with a radio relic in A2163 (Feretti et al. 2001). In A2319, the η pattern with a minimum at $r \simeq 0.07 r_{500} \simeq 100$ kpc suggests enhanced magnetization (see §4) at both small and large radii, possibly implying an intermediate phase between a GH and a MH. Indeed, this halo is associated with both a CF at $r \simeq 100$–200 kpc and a subcluster at $r \simeq 500$ kpc (Govoni et al. 2004), and its clumpy morphology suggests weak magnetization (see §5.1). Note the similar value of η at small and large radii, an order of magnitude apart. The declining $\eta(r)$ profiles of the MHs in Perseus and A2029 are discussed in §5.1.

The X-ray emissivity calculated using the MEKAL model (Mewe et al. 1985, 1986; Kaastra 1992; Liedahl et al. 1995) in XSPEC v.12.5 (Arnaud 1996) is nearly independent of temperature and metallicity,

$$j_{X[0.1-2.4]} \simeq 8.6\times10^{-28} \frac{n_{-2}^2 Z_{0.3}^{0.04}}{T_{10}^{0.1}}\ \mathrm{erg\ s^{-1}\ cm^{-3}}\ , \qquad (4)$$

where n_{-2} is the electron number density n in units of 10^{-2} cm^{-3}, and $Z_{0.3}$ is the metallicity Z in units of $0.3 Z_\odot$. The uniformity of η within each cluster and its universality among different halos (excluding known contaminations) shows nearly equal η in regions spanning two orders of magnitude in density. This implies that the radio emissivity j_ν, like j_X, scales as the gas density squared. Indeed, M09 recently found (in their section 5.1) that assuming $j_\nu \propto n^2$ reproduces the radial profiles of some GHs and MHs.

We examine the temperature dependence of the radio emissivity within a given cluster by fitting η in uncontaminated regions of individual halos as a power law, such that $j_\nu \propto n^2 T^\kappa$ with κ being a free parameter. For A665, A2218 and Perseus, within the radial range $0.25 < r/r_{500} < 0.1$, where no contamination has been identified, we find best fit values $\kappa = -0.42, -0.36$, and 0.84 in each cluster individually, and $\kappa = -0.16$ in the three clusters combined, albeit with low significance. If we include more external, uncontaminated regions, such as the distant parts of A2319, we find that $\kappa = 0.2^{+0.7}_{-1.0}$. The large error bars, few uncontaminated regions, and possible scatter among halos, preclude a better determination of κ with the present data. We note, however, that in each GH region examined we find that $\kappa < 1$ at a confidence level of 95% or higher, and conclude that only $\kappa \lesssim 1$ values are plausible. Additional data could be used to determine κ much more accurately, in particular using the steep temperature gradients found in some MHs. The temperature normalization in Eq. (3) was chosen to approximately match the marginal case $\kappa = 1$.

The scatter in Eq. (3) indicates that the radio emissivity is not a function of the local density and temperature alone. We can represent this by writing $j_\nu = C n^2 T^\kappa$, where the normalization factor C is a function of various cluster properties, such as the mass and the average temperature T_a. It is assumed constant in each halo, but varies with standard deviation $\sigma(\log C) \simeq \log(1.6)$ among the GHs in our sample (*cf.* Eq. (3)). A slightly larger variation, with $\sigma(\log C) \simeq \log(2.5)$, is found if we include the MHs, dominated by the radio brightness of Perseus.

The relatively small variation in C among different GHs and MHs explains the similar volume-averaged emissivity $\langle j_\nu \rangle$ of different GHs, and the high level of variation in $\langle j_\nu \rangle$ among MHs, where $\langle j_\nu \rangle$ is sometimes two orders of magnitude larger than in GHs, as reported by Cassano et al. (2008) and M09. Indeed, the GHs in their sample have comparable sizes and central densities $n_0 \simeq 10^{-2}$ cm^{-3}, whereas the MHs have variable scale and $n_0 > 10^{-1}$ cm^{-3} in some cases.

In addition to the $j_\nu \propto n^2$ dependence, the total radio power of a halo must further increase, on average, with the mass and temperature of the cluster, in order to account for the observed super linear correlation Eq. (1) between the integrated radio and X-ray luminosities. This

could result from a mass or temperature dependence of C or of the halo volume. For example, while the scaling of the radio emissivity with temperature variations *within* each halo is sublinear, $\kappa \lesssim 1$, and the GH data slightly favors a weak, $j_\nu \sim n^2 T^0$ temperature dependence, our sample is consistent with a linear correlation between the total power P_ν of a halo and the average cluster temperature T_a. This would suggest that $C \propto T_a^{\kappa_a}$, where $\kappa + \kappa_a \sim 1$. Generalizing the argument of K09, we use the temperature-luminosity relation observed in clusters, $L_{X[0.1-2.4]} \propto T_a^{\alpha_L}$ with $\alpha_L = 2.0 \pm 0.4$ (Markevitch 1998), to write

$$\nu P_\nu \propto T_a^{\kappa+\kappa_a+0.1} \bar{L}_{X[0.1-2.4]} \propto \bar{L}_{X[0.1-2.4]}^{1+(\kappa+\kappa_a+0.1)/\alpha_L} \ . \quad (5)$$

For $\alpha_L = 2$ ($\alpha_L = 1.6$), $\kappa + \kappa_a \simeq 1.3$ ($\simeq 1.0$) reproduces Eq. (1). Similar results apply for both GHs and MHs, as the temperature-luminosity relation in CCs and in non-cool clusters is similar (*e.g.,* Fabian et al. 1994).

4. UNIVERSAL RADIO MECHANISM

4.1. *Secondary CRE, strong magnetic fields*

The spectral slope near the center of most radio halos is $\alpha \simeq -1$ (see §5.2). A synchrotron spectrum of this type is emitted by rapidly cooling CRE, injected with approximately constant energy per decade in particle energy E_e. The synchrotron emissivity corresponding to a logarithmic CRE energy density injection rate $Q \equiv du_e/(dt\, d\ln E_e) =$ constant is given by

$$\nu j_\nu \equiv \nu \frac{du_\gamma}{dt\, d\nu} = \frac{Q/2}{1+(B_{cmb}/B)^2} \ , \quad (6)$$

where the denominator accounts for Compton losses, $B_{cmb} \equiv 3.2(1+z)^2$ μG is the amplitude of the magnetic field which has the same energy density as the cosmic microwave background, and u_j is the energy density of component j (γ for radio photons, e for CRE, etc.). Combining Eqs. (3), (4) and (6), we obtain a novel constraint on the CRE injection,

$$\frac{Q}{1+(B_{cmb}/B)^2} = 10^{-31.1\pm0.2} n_{-2}^2 T_{10}^{0.9} \text{ erg s}^{-1} \text{ cm}^{-3} \ . (7)$$

As CRE do not have time to diffuse before they lose their energy, this result applies *locally*, in both GHs and MHs.

The remarkably small scatter found in the radio-X-ray correlations among different GHs was previously interpreted as implying a robust radio mechanism that keeps the synchrotron emissivity narrowly distributed around a universal function of the plasma density and perhaps also temperature. Equation (7) and the narrow scatter in its normalization suggest that the universal quantity in radio halos — both GHs and MHs — is $\bar{\eta} \equiv Q(n^2T)^{-1}[1+(B_{cmb}/B)^2]^{-1}$.

Our results strongly emphasize the robustness of the radio emission mechanism. First, we find a tight radio-X-ray correlation not only in GHs but also in MHs. As the latter have physical properties that are considerably different from GHs (smaller size, higher ambient density, nearby AGN, CF association), the radio emission mechanism must be sufficiently robust to reproduce the same levels of $\bar{\eta}$ over a wide range of physical conditions. Second, we confirm that a tight radio-X-ray correlation exists not only in the total cluster luminosities but also in the local brightness, and that this linear correlation is fairly uniform within each cluster. This is particularly striking in MHs, where the coincident density and temperature profiles are steep.

K09 have pointed out that in the strong magnetization regime, defined as $B > B_{cmb}$, radio emission from GHs is independent of the precise value of B, and so the tight correlation only constrains the CRE injection Q. In contrast, in the weak magnetization regime $B < B_{cmb}$, the product QB^2 should be universal, requiring a physical mechanism that carefully balances CRE injection and magnetic fields both with each other and with the ambient gas. Furthermore, in a strongly magnetized halo model, the transition from a constant to a rapidly declining ($\propto B^2$) behavior as B drops below B_{cmb} naturally explains the GH bimodality observed (K09).

The similar values of η we find in GHs and in MHs strengthen this argument considerably, because it is difficult to come up with a double feedback mechanism (CRE–magnetic fields–ambient plasma) that operates identically in the different environments of GHs and MHs, without fine tuning. The bimodality argument does not apply to MHs, however, as their distribution has not been shown to be bimodal, and may in fact be continuous if high magnetization is ubiquitous in CC centers (see discussion in §6.1).

Two types of models have been proposed for CRE injection: *(i)* secondary production by hadronic collisions involving CRI (Dennison 1980); and *(ii)* in-situ turbulent acceleration or reacceleration of primary CRE (Enßlin et al. 1999). These models typically assume fixed ratios between the energy densities of the primary particles (either CRI or CRE), magnetic fields, and thermal plasma $u_{th} \sim nT$. Other possibilities involve a primary CRI distribution that has energy density $u_i \propto n$ (such a scaling is less likely for the magnetic fields or the rapidly cooling CRE), or a magnetic field frozen into the plasma, $B \propto n^{2/3}$. The synchrotron emissivity in each of the nine model variants corresponding to these three primary distributions folded with different magnetization levels and scalings, is shown in Table 2.

TABLE 2
RADIO EMISSIVITY IN MODEL VARIANTS WITH DIFFERENT DISTRIBUTIONS OF CRE AND MAGNETIC FIELDS

	primary CRE $u_e \propto nT$	primary CRI $u_i \propto nT$	primary CRI $u_i \propto n$
$B_{cmb} > B \propto (nT)^{1/2}$	$j_\nu \propto n^2T^2$	$j_\nu \propto n^3T^2$	$j_\nu \propto n^3T$
$B_{cmb} > B \propto n^{2/3}$	$j_\nu \propto n^{7/3}T$	$j_\nu \propto n^{10/3}T$	$j_\nu \propto n^{10/3}$
$B > B_{cmb}$	$j_\nu \propto nT$	$\boldsymbol{j_\nu \propto n^2T}$	$\boldsymbol{j_\nu \propto n^2}$

Among these model variants, only the two secondary CRE models where the magnetic field is strong (models highlighted as boldface in the table) are consistent with the scaling $j_\nu \propto n^2T^\kappa$ where $\kappa \lesssim 1$ and with Eq. (7). Both models are consistent with our data. A slightly better fit to the GH profiles is obtained with $u_i \propto n$ (*i.e.* $\kappa = 0$; see §3), but more data is needed in order to establish the thermal dependence of the CRI distribution with sufficient statistical significance.

An independent argument in favor of these two models is the environment of MHs. MHs are found in re-

laxed clusters such as A2029, where only CFs reveal deviations from hydrostatic equilibrium. Such CFs reflect subsonic bulk shear flows and strong magnetization, but were not associated with particle acceleration. The CF-MH connection therefore supports both secondary CRE and strong magnetization in MHs. The similarity in the values of η we find in GHs and in MHs implies, transitively, that the same holds for GHs.

Additional evidence supporting the presence of strong magnetic fields and the absence of primary CRE is found by examining the morphological and spectral properties of halos, as discussed in §5. Notice, for example, that the brightness correlation shown in Fig. (2) is strongest in the centers of halos, but diminishes at larger radii, where turbulent activity associated with mergers is expected and where merger shocks and relics are found (*e.g.,* in A665 and A2163). In primary CRE models, one would not expect the correlation to preferentially tighten *away* from the turbulent regions.

4.2. *Temporal variations*

The preceding discussion is strictly valid only as long as the timescale for substantial changes in the magnetic field is longer than the cooling time of the CRE, t_{cool}. For CRE that emit synchrotron radiation received with characteristic frequency ν,

$$t_{cool} \simeq 0.13 \left[\frac{4\left(\frac{B\sqrt{3}}{B_{cmb}}\right)^{-3/2}}{1+\left(\frac{B}{B_{cmb}}\right)^{-2}} \right] \nu_{1.4}^{-\frac{1}{2}} (1+z)^{-\frac{7}{2}} \text{ Gyr} \ , \quad (8)$$

where the term in square brackets peaks at unity when $B = B_{cmb}/\sqrt{3}$, and scales as $B^{-3/2}$ for $B \gg B_{cmb}$. In GHs, t_{cool} is much shorter than the $\gtrsim 1$ Gyr timescale characteristic of the halo lifetime (K09).

However, significant local variations in the magnetic field can take place on a shorter timescale, of the order of the sound crossing time of the turbulent eddies, $t_s \sim l/c_s$. This is shorter than t_{cool} for a sound velocity $c_s \sim 10^3$ km s^{-1} and eddy length scales $l \lesssim 100$ kpc. (Note that substantial magnetic power is measured on coherence scales ~ 10 kpc; see §6.1.) The radio emission should therefore be averaged over t_{cool} and over the beam. Nevertheless, as long as many eddies contribute to the emission, and the variations in magnetic energy density remain of order unity, this correction would be small. Notice that fast changes in magnetic configuration over a *light* crossing time, if present, may be observed as temporal radio variations by next generation telescopes such as SKA. Indeed, the milli-arcsecond resolution attainable by SKA (Schilizzi et al. 2007) corresponds to a light-crossing time of less than a year, for nearby halos at redshift $z \lesssim 0.02$.

In MHs, the magnetic fields are probably associated with sloshing activity in the core (see §6.1). The characteristic timescale for the decay of core sloshing is $\gtrsim 1$ Gyr (*e.g.,* Ascasibar & Markevitch 2006), much longer than t_{cool}. The timescale for the buildup of sloshing depends on its trigger mechanism; in a merger induced scenario this is again $\gtrsim 1$ Gyr. However, local variations in the magnetic field could occur over the radial sound crossing time, $t_s \sim r/c_s$, or on the crossing time of the magnetic structures associated for example with CFs. These timescales could be shorter than t_{cool} in the central ~ 50 kpc (note that in these regions B usually significantly exceeds B_{cmb}; see §5.1). As in GHs, averaging over t_{cool} and over the beam could introduce small variations in radio brightness, in particular at the edges of MHs.

Notice that in both GHs and MHs, $\bar{\eta}$ is only weakly sensitive to variations in CRE injection, and only through changes in the fractional energy of the CRI, u_i/u_{th}. Thus, $Q/(n^2T^{0.9})$ should be replaced by its value averaged over t_{cool} and over the beam. This correction should be very small, except possibly near a CRI source.

5. SIGNATURE OF SECONDARY CRE IN STRONG FIELDS

A model invoking secondary CRE in strong magnetic fields as the origin of radio halos implies particular morphological and spectral properties of GHs and MHs. These properties can be used to shed light on halo observations, to test the model, and to gauge its parameters. In particular, the distributions of CRE and magnetic fields can be measured separately, and not only their degenerate product as in other models.

5.1. *Morphology: $B < B_{cmb}$ radio suppression*

In our model, both GHs and MHs are regions in which strong magnetic fields with $B > B_{cmb}$ indirectly illuminate the cluster's CRI population in radio waves. More than half of all CCs contain CFs. Beneath the CFs, bulk shear flow magnetizes the plasma; there is however no evidence for shear above the CFs (Keshet et al. 2009). Therefore, the sharp termination of some MHs coincident with CFs is naturally expected. This is probably the reason for the rapid, nearly exponential $\eta(r)$ cutoff in Perseus above $r \simeq 0.05 r_{500} \simeq 50$ kpc, shown in Fig. 2. Note that CFs are not spherical; the radial decay may result from one or several CFs extending over various radii, seen projected and radially binned.

In GHs, and in MHs away from CFs, it is natural to assume that the magnetic field decays with r, possibly as some fixed fraction of equipartition, $B^2 \propto nT$. At some distance r_b, B drops below B_{cmb}, leading to a $(B/B_{cmb})^2$ suppression in the radio emissivity. This can produce a radial break in the projected radio profile, with $\eta \simeq$ constant at $r \ll r_b$, and $\eta \propto B^2 \propto r^{\kappa_B}$ at $r \gg r_b$ with some $\kappa_B < 0$. A power-law pressure profile $nT \propto r^{\kappa_P}$ would imply $\kappa_B = \kappa_P$; for an isothermal distribution $\kappa_B = -2$.

Such a break is found in A2029 at $r_b \lesssim 120$ kpc, as seen in Fig. 2 (diamonds). The figure also shows a simple model (dashed curve) where we assume that $B^2 = knT$ and that η asymptotes to its average GH value at small radii, $\eta(r \to 0) \to 10^{-4.3}$. We adopt a best fit cusp $\beta-$model (Lewis et al. 2003), assuming a uniform temperature (indeed, T varies by less than 10% in the relevant region; Snowden et al. 2008), so the proportionality constant k is the only free parameter. This yields a reasonable fit, with $B = 3.2$ μG at $r \simeq 0.09 r_{500} \simeq 110$ kpc and $B \simeq 10$ μG at $r = 10$ kpc. Similar results are obtained with β (Chen et al. 2007), double-β (Lewis et al. 2003), and composite (Vikhlinin et al. 2006) density models.

Assuming that $B^2 \propto nT$ for $r < r_b$, we can place a lower limit on the central magnetic field amplitude B_0 in

each observed halo. If no break in η is identified out to radius R_ν, then

$$B_0 > B_{0,min} \equiv \left[\frac{(nT)_{r=0}}{(nT)_{r=R_\nu}}(f_{ic}^{-1}-1)\right]^{1/2} B_{cmb}(z)\ , \quad (9)$$

where we allowed a fraction $f_{ic} \simeq 0.5$ of inverse Compton losses at R_ν. The $B_{0,min}$ values of the halos in our sample are presented in Table 1, assuming individual isothermal β-models for each cluster as detailed in the table. In the MHs, the central magnetic field could be much higher than $B_{0,min}$ because *(i)* the significant growth in nT towards the center (due to the density cusp) is not captured by the β-model; and *(ii)* the magnetic field immediately beneath the CFs could be very strong, $B \gtrsim 17$ μG (Keshet et al. 2009).

Instead or in addition to a radial break in brightness, a halo in which the magnetic field is marginal, $B \simeq B_{cmb}$, could become clumpy or filamentary, appearing bright only in $B \gtrsim B_{cmb}$ islands. This is probably the reason for the unusual clumpy or filamentary radio morphology observed in RXC J2003.5-2323 (Giacintucci et al. 2009), A2255, and A2319 (M09). Indeed, a decline in η is directly seen in A2319 around $r = 100$ kpc (suggesting low magnetization; see Fig. 2), and A2255 is the only strongly (20%–40%) polarized GH known todate (Govoni et al. 2005); the absence of strong beam depolarization suggests relatively weak magnetic fields (see, for example, Murgia et al. 2004). Additional evidence for the low magnetization in these three halos is their relatively steep spectrum, as discussed in §5.2.

Such marginally magnetized halos are particularly interesting because the magnetic field can be determined in multiple locations, and because the radio morphology directly gauges the magnetization or magnetic decay process. Fast putative variations in the magnetic field may be easier to detect in such regions, as they could involve temporal changes in the small scale radio morphology. For example, in A2319, SKA could resolve such changes over a light-crossing time of ~ 2 years.

While radio emission rapidly declines outside the $B > B_{cmb}$ region, an opposite signature is expected in inverse-Compton emission from the same CRE, as they scatter CMB photons to high energies. This emission may be clumpy or filamentary in $B \sim B_{cmb}$ regions. However, as pointed out by Kushnir & Waxman (2010), such radiation cannot explain the hard X-ray excess detected in a number of clusters (for review, see Rephaeli et al. 2008), because the inverse Compton signal from secondary CRE has νI_ν comparable to that in the radio (see Eq. (3)), ~ 3 orders of magnitude lower than needed to account for the detected hard X-ray excess.

5.2. *Using the radio spectrum to measure CRI and magnetic fields*

Spectral steepening with increasing r, increasing ν, or decreasing T, has been reported in several radio halos (Feretti & Giovannini 2008; Ferrari et al. 2008; Giovannini et al. 2009, and references therein). Such trends naturally arise in our model, due to the energy-dependence of the inelastic cross-section for collisions of CRP with the intracluster gas at the relevant $E_p \sim 20$ GeV CRP energies.

Secondary CRE are mainly produced by charged pion production, $p + p \rightarrow \pi^\pm + X$, where X is any combination of particles, followed by mesonic decays $\pi^\pm \rightarrow \mu^\pm + \nu_\mu(\bar{\nu}_\mu)$ and leptonic decays $\mu^\pm \rightarrow e^\pm + \nu_e(\bar{\nu}_e) + \bar{\nu}_\mu(\nu_\mu)$. Other processes, in particular He-p collisions, have a similar cross-section per nucleon and should not modify our results by more than 10%. On average, the energies of the CRE, the $\pi^\pm$, and the CRP are related by $E_e \simeq f_{e|\pi}E_\pi \simeq f_{e|\pi}f_{\pi|p}E_p$, where $f_{e|\pi} \simeq 1/4$ and $f_{\pi|p} \simeq 1/5$ (Ginzburg & Syrovatsky 1961). The inclusive cross section for $\pi^\pm$ production varies significantly as a function of E_p around $E_p \simeq 10$ GeV, dropping from > 40 mb above 30 GeV to zero at the threshold energy 0.3 GeV (Blattnig et al. 2000).

We compute the radio spectrum based on two different methods. Model A uses the spectral fits for e^+ and e^- production in inelastic p-p scattering according to Kamae et al. (2006, valid for 0.5 GeV $< E_p <$ 512 TeV), with corrected parameters and cutoffs (T. Kamae & H. Lee, private communication). Model B assumes that $E_e = (E_p/20)$ and utilizes the inclusive cross sections for charged pion production according to Blattnig et al. (2000), which agree with experimental data for $0.3 < (E_p/\mathrm{GeV}) \lesssim 300$ (Norbury 2009). Model A should be more accurate, because $f_{e|\pi}f_{\pi|p}$ is not independent of E_e and the CRP spectrum.

The results, depicted in Fig. 3 for emitted frequency $\nu_e = (1+z)\nu = 1.4$ GHz and various power-law CRP spectra $n_p(E_p) \propto E_p^s$, show that the radio spectrum steepens with increasing electron/positron energy,

$$E_e \simeq 4.2\nu_{e,1.4}^{1/2}(B/5\ \mu\mathrm{G})^{-1/2}\ \mathrm{GeV}\ . \quad (10)$$

Model A features a spectral break at $E_e \simeq 2$ GeV, attributed mainly to electron production through diffractive processes, in which one or both protons transitions to an excited state (discrete resonances and continuum). Note that even if this channel is blocked, a similar spectral break is found at $E_e \sim 1$ GeV. A more dramatic steepening than in either model is found if we assume that $E_e = (E_\pi/4)$ and use the pion spectra produced in p–p collisions according to Blattnig et al. (2000); however, these formulae have not been tested beyond $E_p = 50$ GeV.

Due to the limited energy range over which the energy index $s_e \equiv d\log(n_e)/d\log(E_e)$ of the injected CRE can be computed, the radio spectrum in Fig. 3 is calculated in the approximation where each CRE emits a single photon, such that $\alpha \simeq s_e/2$ (*e.g.,* Keshet et al. 2003). A more accurate computation, convolving the CRE distribution with the synchrotron emission function, would somewhat smear the spectral features.

The radio steepening with increasing E_e implies steepening with increasing ν or r, or decreasing T, as observed. Both models agree that spectral steepening by $|\Delta\alpha_\nu| > 0.2$ indicates $B > 20(\nu_e/1.4\ \mathrm{GHz})$ μG magnetic fields in the region associated with a flatter radio spectrum. Measuring α at the spatial ($B \simeq B_{cmb}$) or spectral ($E_e \simeq 2$ GeV) breaks, can be used to measure the CRP spectrum s, as illustrated in the inset of Fig. 3. Conversely, if a distinct spectral break exists as predicted by model A, it would directly gauge the magnetic field, once the CRP spectrum has been determined. Multi-frequency radio data could thus allow a sensitive mapping of the magnetic field, both above and below B_{cmb},

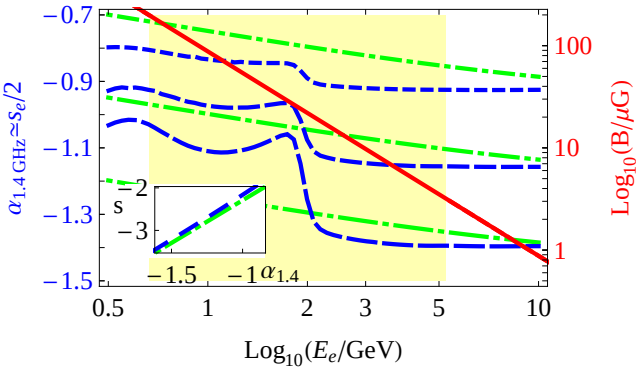

FIG. 3.— The relation between α (dashed curves; left axis), B (solid curve, right axis) and E_e, for $\nu_e = 1.4$ GHz. The highly magnetized, $B_{cmb}(z=0) < B < 200\ \mu$G regime is shaded. The radio spectral index $\alpha_{1.4}$ is shown as a function of E_e according to model A (dashed) and model B (dash-dotted), for CRP spectral indices $s = -2$, -2.5, and -3 (top to bottom). See §5.2 for model and parameter description. *Inset*: The CRP energy index s as a function of radio spectral index $\alpha_{1.4}$, at the spatial halo break where $B = B_{cmb}$ (see §5.1).

throughout the cluster, for example using deprojected maps at several radio frequencies.

Spectral measurements of radio halos should be interpreted with caution. Contamination by CRE sources such as shocks, relics, central AGNs, and radio galaxies, is common. Spatial averaging often blends together different sources, depending on flux sensitivity and angular resolution. Therefore, with present observations, the spectrum can be reliably associated with a halo only when measured locally in uncontaminated regions; in our model these are regions of uniform η. Also note that radio emission above 1 GHz is increasingly suppressed by the Sunyaev-Zel'dovich effect (Enßlin 2002).

For example, the regular GH in A2744 exhibits a linear radio-X-ray correlation in brightness (Govoni et al. 2001a). Along the main NW elongation, the 0.3 − 1.4 GHz spectral slope $\alpha(r < 200\ \mathrm{kpc}) \simeq -1.0$, slightly flattens to -0.9 around 500 kpc, and steepens again to -1.5 as $r \to 1$ Mpc. An azimuthal average, however, includes a NE relic tail and under-threshold regions, leading to an unrealistically uniform $\alpha(r < \mathrm{Mpc}) \simeq -1$ (Orrú et al. 2007). A similar behavior is found in A2219 (Orrú et al. 2007). Steepening from $\alpha \simeq -1.0$ to $-$(1.2-1.5) in the less perturbed direction was also found in A665 (partly overlapping the $r < 0.13 r_{500}$ flat η region seen in Fig. 2, where α steepens from -1.0 to -1.2), A2163 (Feretti et al. 2004b), and Coma (Giovannini et al. 1993).

Comparable steepening was found as a function of frequency in the GH in A754. Its spectrum measured between 74 and 330 MHz, $\alpha_{0.07}^{0.3} \sim -1.1$, steepens to $\alpha_{0.3}^{1.4} \sim -1.5$ (Bacchi et al. 2003). More substantial steepening has been reported in other clusters, such as A2319 (Feretti et al. 1997) and A3562 (Giacintucci et al. 2005). However, contamination by extended radio galaxies was reported in all these halos.

Significant steepening with increasing r or ν as in the examples above is more consistent with the $E_e \sim 2$ GeV spectral break of model A than with model B. In model A, strong magnetic fields with $B \gtrsim 10(\nu_e/700\ \mathrm{MHz})\ \mu$G are present in regions where α_ν is flat. Moreover, an uncontaminated spectral break measured at some emitted frequency ν_b would imply that the local projected magnetic field is $B \simeq 10(\nu_b/700\ \mathrm{MHz})\ \mu$G. Observations at several frequencies can thus be used to map the local projected magnetic field. As a preliminary example, interpreting the radio spectrum of A754 as a spectral break somewhere between $\nu_e = 200$ and 900 MHz near the center of the halo, would imply $3 < B_0/\mu\mathrm{G} < 14$.

Figure 3 indicates that radio steepening from $\alpha = -1.0$ to -1.3 corresponds to a CRP spectral index $s \simeq -2.7$. Steepening beyond -1.5, if uncontaminated, would imply a steep CRP spectrum with $s < -3$. The radio spectrum at high, $E_e \gg 10$ GeV CRE energies approaches $\alpha \to s/2$. However, inward of the spectral break, at $E_e < 2$ GeV, $\alpha \simeq -1$ depends only weakly on s. This could explain the universally observed $\alpha \simeq -1$ in the centers of halos.

Figure 4 shows the average $\nu \lesssim 1.4$ GHz spectral indices $\langle\alpha_{1.4}\rangle$ reported for GHs in our sample, as a function of their minimal central magnetic fields $B_{0,min}$ calculated in §5.1. The results are also summarized in Table 1. A positive correlation is seen, in the sense that halos with stronger central magnetization tend to have a flatter radio spectrum, as expected. Note that this correlation is stronger than, and not simply due to, a correlation we find between $\langle\alpha\rangle$ and the halo size.

For comparison, we also plot (dashed lines in Fig. 4) the average radio spectrum $\langle\alpha_{1.4}\rangle$ as a function of B_0, computed for a typical isothermal β-model with $\beta = 0.7$, assuming $B^2 \propto nT$, spectral model A, and radio emission extending to $R_\nu \simeq 3r_c$. Although this result cannot be quantitatively compared to the GH data (which are only lower limits on B_0), the trends qualitatively agree. This provides an independent indication that the CRP spectrum is steep, with $s \lesssim -2.7$.

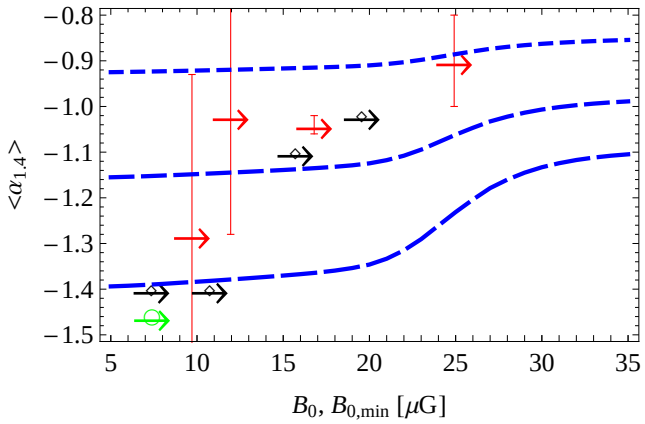

FIG. 4.— The relation between the spatially averaged, $\nu \lesssim 1.4$ GHz spectral index $\langle\alpha_{1.4}\rangle$, and the central magnetic field B_0. The measured spectral index in each GH is plotted as a function of the minimal central magnetic field $B_{0,min}$ calculated in §5.1 (right arrows; data with no reported error bars shown as diamonds; data with error bars larger than the y-axis shown as a circle; see Table 1). Also shown (dashed curves) is the average spectrum calculated in a simple magnetic equipartition, isothermal β-model (see §5.2), as a function of the central magnetic field, for CRP energy indices $s = -2$, -2.5, and -3 (top to bottom).

The radio spectrum is relatively steep in the five GHs and MHs for which we presented evidence for low magnetization in §5.1, in agreement with the $\langle\alpha\rangle - B_0$ correlation. These halos, which are not shown in Fig. 4,

include A2029 ($\langle\alpha_{0.2}\rangle \simeq -1.35$, Slee & Siegman 1983), A2255 ($\langle\alpha_{0.3}^{1.4}\rangle = -2.06 \pm 0.57$, Kempner & Sarazin 2001, where we infer $\langle\alpha_{0.6}^{1.4}\rangle \sim -1.5$ by comparing M09 with Harris et al. (1980)), A2319 ($\langle\alpha\rangle = -1.28^{+0.35}_{-0.35}$, Kempner & Sarazin 2001), Perseus ($\langle\alpha_{0.3}^{1.5}\rangle \sim -1.2$, Gitti et al. 2004), and RXC J2003.5-2323 ($\langle\alpha_{0.2}^{1.4}\rangle \sim -1.32 \pm 0.06$, Giacintucci et al. 2009).

Finally, a cautionary comment is in place regarding the extrapolation of the spectrum to low frequencies that correspond to $E_e \lesssim 1$ GeV CRE energies. Although $E_e = 1$ GeV CRE are produced on average by $E_p \sim 20$ GeV CRP (for $s = -2.5$), the contribution of low energy CRP with $E_p \lesssim 3$ GeV is not negligible. We expect a CRP power law energy spectrum $n_p(E_p) \propto E_p^s$ to be modified around the proton rest mass. Consequently, our s = constant approximation becomes increasingly unlikely at low, $E_e \lesssim 1$ GeV CRE energies.

6. DISCUSSION: ORIGIN OF CRI AND MAGNETIC FIELDS

After motivating a model invoking secondary CRE and strong magnetic fields as the source of radio halos in §4, and discussing the implications of such a model in §5, we now consider the origins of the magnetic fields (§6.1) and of the primary CRI (§6.2). We subsequently summarize our results in §6.3.

6.1. *Magnetization: mergers (GHs) and sloshing (MHs)*

In the model derived above, the primary CRI population is long-lived and has very similar properties in different clusters and in different parts of a cluster. Hence, the defining property of halos is sufficiently high magnetization. Measuring strong, $B > B_{cmb}$ magnetic fields without radio detection at the level given by Eq. (3) would rule out the model, unless the CRI energy fraction is exceptionally low (*e.g.,* due to a very low level of star formation; see §6.2). The model can be tested by checking if the different magnetic field estimates it produces in a given halo are self consistent, and agree with independent measurements.

In the model, GH clusters are associated with strong, $B \gtrsim B_{cmb} \sim 3$ μG magnetic fields, whereas weaker, $B < B_{cmb}$ fields are present in clusters devoid of a halo. Magnetic fields of the order of B_{cmb}, extending over Mpc scales, are consistent with Faraday rotation measures (RM) in non-cool clusters, considering the uncertainties involved. Such RM studies suggest magnetic fields ranging between a few μG to 10 μG, extending out to $r \sim 500$ kpc, in a sample of non-cool core clusters, on 10–20 kpc coherence scales (Clarke 2004). Weaker magnetic fields, typically ~ 1 μG to a few μG, were found using other methods, such as simulating the polarization of extended sources (Murgia et al. 2004) or using a Bayesian maximum likelihood analysis of the Faraday RM (Vogt & Enßlin 2005).

RM studies could potentially test the association between strong magnetization and the presence of halos, as implied by the model, although this is complicated by several factors. First, RM analyses involve substantial systematic and statistical errors associated with projection effects, the magnetic power spectrum, the range of coherence scales, and non-Gaussianity. Second, cluster fields are often reconstructed using peripheral RM sources, assuming some magnetic field scaling $B \propto n^{\mu}$ that extends both inside and outside the halo; however this assumption is uncertain and in some cases inconsistent with our model, *e.g.,* in asymmetric or clumpy halos. Third, the RM gauges the magnetic field amplitude integrated along the line of sight, whereas the radio emission scales differently with the magnetic field, *e.g.,* as B^2 in $B \lesssim B_{cmb}$ regions. Finally, magnetic estimates for different clusters should be compared under similar assumptions. For example, assuming a Gaussian, Kolmogorov magnetic power spectrum with $\mu = 1/2$, we find $\langle B(r < 3r_c)\rangle = 1.8$ μG and $B(3r_c) = 1.3$ μG in Coma (Bonafede et al. 2010), which harbors a GH, while weaker fields, $\langle B(r < 3r_c)\rangle = 1.2$ μG and $B(3r_c) = 0.8$ μG are found in A2382 (Guidetti et al. 2008), which has no halo. Similarly, $\langle B(r < 3r_c)\rangle = 1.3$ μG and $B(3r_c) = 0.8$ μG are found in A119 (Murgia et al. 2004), which does not harbor a GH, but this result is obtained for $\mu = 0.9$ so comparison to the other two clusters may be misleading. Note that it is not clear, considering the inherent uncertainties, if the differences between these B estimates are significant.

The association between GHs and merger events is fairly well established (see Feretti & Giovannini 2008, and references therein). With present magnetic field estimates, it is quite plausible that a major merger event could amplify the intracluster magnetic field by a factor of a few, sufficient to exceed B_{cmb} and produce a GH. The model thus resolves the notorious discrepancy between magnetic field estimates based on Faraday RM and on previous GH analyses, which unnecessarily assumed equipartition between magnetic fields and CRE.

The very strong magnetic fields we infer in the centers of MHs are consistent with the RM observed in CCs, which typically imply $B \simeq 10 - 40$ μG in the core, on coherence scales of a few up to 10 kpc (Carilli & Taylor 2002). It is interesting to point out that the cooling flow power is correlated both with the RM (Taylor et al. 2002) and with the MH radio power (Gitti et al. 2004), while no strong correlation between MH and AGN power was identified (*e.g.,* Govoni et al. 2009).

The association between MH edges and CFs strongly suggests that sloshing motions play a major role in magnetizing the core. Notice that ~ 10 kpc scales are indeed characteristic of the shear magnetic amplification anticipated beneath CFs (Keshet et al. 2009). Sloshing could suppress cooling in the core, for example by mixing the cold gas with a heat inflow (Markevitch & Vikhlinin 2007). In such a scenario, a stronger cooling flow may correspond to a larger magnetized region, leading to correlations between the cooling flow power and both RM and MH power, as observed, but not necessarily to an MH-AGN correlation.

The distribution of MHs (without the AGN component) among CCs should reflect the statistics of core magnetization, and therefore of sloshing. We expect a correlation between the presence of MHs and of CFs in a cluster, and a correlation between the MH size or power and the shear flow strength, manifest for example in the number and size of CFs and in the (measurable, see Keshet et al. 2009) shear across them. Assuming that some level of magnetization by core sloshing is always present in CCs, as suggested by the ubiquity of observed CFs, the steep magnetic profile associated with the density cusp would imply that all CCs have some MH, even

if small. The MH distribution would then be continuous, and not bimodal as in GHs.

Shear amplification of magnetic fields parallel to the CF plane is expected mostly below the CF and in a thin boundary layer around it, in which the field can reach high, near equipartition levels (Keshet et al. 2009). The morphological association between MH edges and CFs, discovered by Mazzotta & Giacintucci (2008), is therefore expected to be ubiquitous. It is best seen where CFs are observed edge on; elsewhere it may be observed as morphological correlations between radio maps and spatial X-ray gradients, which trace projected CFs.

The magnetic field (the polarization) is expected to be parallel (perpendicular) to the CF, *i.e.* approximately tangential (radial). Polarization would be preferentially observable where beam deprojection is minimal, *i.e.* at large radii where the magnetic field weakens. Interestingly, nearly radial, $10\%-20\%$ polarization was detected in the MH in A2390, growing stronger with increasing radius (we refer to the spherical, $r\sim 150$ kpc component around the cD galaxy in this irregular MH; see Bacchi et al. 2003). We predict that near CF edges, where the magnetic field is particularly strong, the radio spectrum would be relatively flat (see §5.2).

6.2. *CRI Origin: diffusion and supernovae sources*

The spectral steepening of the radio signal with increasing CRE energy $E_e\propto(\nu/B)^{1/2}$, provides a novel method for measuring the primary CRP spectrum. The radio steepening observed in some halos, roughly from $\alpha\simeq-1.0$ to $\alpha\simeq-1.3$, corresponds to a CRP spectral index $s\lesssim-2.7$ at $E_p\sim 20$ GeV energies. The CRP energy fraction then becomes (*cf.* Eq. 7)

$$\xi_p(>E_p)\equiv\frac{u_p(>E_p)}{u_{th}}\simeq 10^{-3.6\pm0.2}\left(\frac{E_p}{10\text{ GeV}}\right)^{-0.7} \quad (11)$$

Note that with the uncertain and possibly contaminated radio spectra presently available, a steeper CRP spectrum with $s\simeq-3$ is possible. The model could probably be ruled out if the *uncontaminated* spectrum of a substantial halo population turns out to be much steeper than $\alpha=-1.5$, unless the corresponding steep CRP spectrum can be explained.

The CRP distribution in Eq. (11) resembles (but has an energy fraction a few 100 times smaller than) the CRP distribution found in the solar vicinity above 1 GeV/nucleon. This distribution could originate from sources that inject roughly equal energy per decade of CRP energy ($s_0\simeq-2.2$), such as supernovae (SNe), if energy-dependent diffusion is significant in the inner halo regions. For example, a simple estimate of CRI scattering off magnetic irregularities with a Kolmogorov power spectrum yields a diffusion coefficient $D\simeq 10^{30}(E_p/\text{GeV})^{1/3}(B/\mu\text{G})^{-1/3}$ cm^2 s^{-1} (Völk et al. 1996). This implies CRI diffusion over ~ 0.5 Mpc during a Hubble time, and a steepening by $\Delta s=-1/2$. More substantial steepening is possible if the diffusion function has a stronger energy dependence. For example, the diffusion function is often assumed to scale as $D\propto E_p^{1/2}$, which could lead to a $\Delta s=-3/4$ steepening in the CRI spectrum.

The CRI output of SNe can be crudely estimated (Völk et al. 1996) if we assume that a fraction $f_{\rm II}$ of the cluster's $Z=0.3Z_{0.3}$ solar metallicity is seeded by Type II SNe, which on average produce $0.1M_\odot M_{Fe,0.1}$ of iron and deposit a fraction $\xi=0.3\xi_{0.3}$ of the $10^{51}E_{51}$ erg explosion energy in $E_p>10$ GeV CRI,

$$\xi_p^{SN}\simeq 0.03 f_{\rm II}Z_{0.3}E_{51}M_{Fe,0.1}^{-1}\xi_{0.3}\ . \quad (12)$$

This can reproduce Eq. (11) if over the cluster's lifetime, the CRI diffuse to distances a few times larger than the radius R_ν of the radio halo. Note that if CRI diffusion is entirely absent, the CRI accelerated in SNe would be confined to the cluster, and adiabatic losses could only lower their energy density to the level of Eq. (11). However, they would then retain their flat, $s\simeq-2.2$ spectrum.

An SNe origin of CRI can be tested by examining the correlations between η and (intensive) tracers of SNe activity among different halos. One possible tracer is the local metallicity measured at $r=0.1r_{500}$, tabulated in Table 1. We chose to use $Z(0.1r_{500})$ because *(i)* it was measured for all the M09 halos with XMM profiles in Snowden et al. (2008); *(ii)* the spatially averaged Z is not meaningful when temperature gradients are large; and *(iii)* $0.1r_{500}$ lies well within the $Z(r>0.02r_{500})\propto r^{-0.3}$ decline typically found in both cool and non-cool core clusters (Sanderson et al. 2009). While our sample is statistically small, Perseus, which shows a significantly higher η than in all the other halos in our sample, also shows a slightly higher $Z(0.1r_{500})$ (Snowden et al. 2008). However, due to the large uncertainty in abundance measurements, the elevated metallicity in Perseus is not significant ($<1\sigma$) with respect to some halos. Moreover, at smaller radii $r\lesssim 0.025r_{500}$, the metallicity in A2029 appears to be higher than in all other halos, and is significantly ($>3\sigma$) higher than in Perseus (Snowden et al. 2008).

Although better metallicity statistics may identify some correlation between η and Z, metallicity is probably not the most useful tracer of the SNe contribution to CRI in the halo. Metallicity provides a cumulative measure of SNe activity, tracing the metals released from all past SNe in the cluster. In a model where a significant fraction of the CRI have already diffused away from the cluster's center, metallicity would not linearly trace the population of CRI residing within the halo, especially in the more compact MHs. It is more appropriate to use an intensive tracer of *recent* SNe activity, such as the star formation rate (SFR) normalized by the cluster's gas mass M_g, or the fraction of star forming galaxies. A correlation between an SNe measure and a CRI tracer, such as η or the deviation from the luminosity correlation $\nu P_\nu/\bar{L}_{X[0.1,2.4]}^{1.7}$, may be more useful than the metallicity in establishing or ruling out an SNe origin of halo CRI.

As seen in Fig. 2, the uncontaminated regions in seven out of the nine halos in our sample are consistent with an identical η value, $\eta\simeq\eta_0\equiv 10^{-4.3}$. The two remaining halos are relatively radio bright; the MH in Perseus has $\eta\sim 7\eta_0$, and the GH in A665 has $\eta\sim 1.6\eta_0$. Interestingly, there is evidence for exceptionally high specific star formation in both Perseus and A665.

In Perseus, which has the smallest M_g (by at least a factor of 4, see Fukazawa et al. 2004) and one of the most powerful cooling flows within our sample (*e.g.,* White 2000; Allen et al. 2002), there is optical-to-UV evidence for a relatively high SFR (*e.g.,* Bregman et al. 2006; Raf-

ferty et al. 2008). In particular, the cD galaxy NGC1275 in Perseus has a high SFR of $\sim 30 M_\odot$ yr^{-1} (Dixon et al. 1996) — the highest in our sample when normalized by M_g. Notice that the central galaxy in A1835 has a higher SFR of $\sim 100 M_\odot$ yr^{-1} — the highest SFR known in such objects (Peterson & Fabian 2006). However, M_g is ~ 10 times larger in A1835 with respect to Perseus (Fukazawa et al. 2004). Note that high cosmic-ray density regions are directly observed in Perseus in the form of X-ray cavities, reaching distances $r > 100$ kpc (M. Markevitch, private communications). A665 was found to be the cluster with the highest dispersion in color magnitude relation (a known tracer of star formation) in a sample of 57 X-ray bright clusters (López-Cruz et al. 2004).

While these trends support an SNe origin of CRI, more work is needed in order to quantify their significance and compile a comparative statistical analysis. Note that the combination of a strong correlation of η with the specific SFR and a poor correlation with metallicity, if established, would directly imply that CRI diffusion is significant. Indeed, it is difficult to explain the steep, $s \lesssim -2.7$ spectrum without invoking CRI diffusion. The above estimates of diffusive steepening Δs assume that most of the CRI produced by the sources presently dominating the halo have already escaped beyond it. This is consistent with the typical SFR peak at $z \sim 1$, and with the above estimates of the halo CRI abundance and the total CRI output of SNe (*cf.* Eqs. 11 and 12). However, such substantial diffusion would introduce some scatter in the radio–X-ray correlation, depending on the CRI production history of each cluster. Quantitative estimates of the SNe history of GH clusters, needed to compute this scatter, are beyond the scope of this work.

6.3. *Summary and Conclusions*

We have shown that the radio-X-ray correlation in GH luminosity (Eq. 1) can be generalized (Eq. 2) to hold for both GHs and MHs (Fig. 1), by correcting for the halo size. A universal, local radio-X-ray correlation in brightness was presented (Eq. 3 and Fig. 2), implying that the radio emissivity (Eqs. 6-7) scales as $j_\nu \simeq C n^2 T^\kappa$, where $\kappa \lesssim 1$ and the coefficient C varies little among different halos. We argued that these results and their applicability to GHs and MHs alike, strongly supports one model for all halos, involving secondary CRE (injected according to Eq. 7) and strong magnetic fields with $B > B_{cmb}$, while disfavoring other models (Table 2).

This model makes useful predictions without requiring additional assumptions or fine tuning. Radio emission rapidly fades in regions where B drops below B_{cmb}, producing a distinct radial break (*e.g.,* in A2029 and in Perseus; Fig 2) or a clumpy/filamentary radio morphology (*e.g.,* in RXC J2003.5-2323, A2255, and A2319) that can be used to map $B \simeq B_{cmb}$ contours. Marginally magnetized regions with $B \lesssim B_{cmb} \propto (1+z)^2$ are characterized by relatively high polarization and a steeper radio spectrum; their morphology traces the magnetic evolution and can potentially reveal a temporal signal. We expect a higher incidence rate of such transition regions at higher redshift, while no halos should exist at very high redshift.

Another direct consequence of the model is radio spectral steepening with increasing $E_e^2 \propto \nu/B$ (Eq. 10), *i.e.* with increasing r or ν or decreasing T, as indeed is observed. Such steepening, and in particular a $B \simeq 10(\nu_e/700\ \mathrm{MHz})\ \mu$G spectral break (Fig. 3), gauges the magnetic field, roughly producing an additional B contour for each radio map frequency. The spectral break could be used to accurately map B throughout the halo, using future radio telescopes such as MWA[3], LOFAR[4] and SKA.

A pressure model can be used to extrapolate B throughout the cluster. This indicates central magnetic fields B_0 (Eq. 9) that exceed 10 μG in most halos (see Table 1 for lower limits $B_{0,min}$). A correlation between the average radio spectral index $\langle\alpha\rangle$ and B_0, implied by the model, was identified in GH data (Fig. 4).

In our model, any source of strong ($B > B_{cmb}$), persistent magnetic fields in the intracluster medium would have similar properties to radio halos, as long as it does not significantly inject additional cosmic rays. This may include some extended radio galaxies, which were recently found to exhibit properties similar to halos (Rudnick & Lemmerman 2009). Conversely, the universal value of η we predict for any highly magnetized region in the intracluster medium (uncontaminated by a recent shock) provides a powerful test of the model.

The spectral steepening of the radio signal, the universality of $\alpha \simeq -1$ in the centers of halos, and the correlation between $\langle\alpha\rangle$ and $B_{0,min}$ (Fig. 4), indicate a steep CRI spectrum, $s \lesssim -2.7$, and thus favor significant CRI diffusion. In a diffusion model, the most plausible source of the CRI (Eq. 11) is SNe (*e.g.,* Eq. 12). We show (in §6.2) preliminary evidence for a correlation between η and the SFR normalized by the gas mass M_g, supporting an SNe CRI origin. None of these properties is expected in an alternative model (K09), in which the secondary CRE arise from ~ 1 GeV CRP, which are accelerated in the cluster's virial shock and advected inward with the flow, thus being compressed to ~ 10 GeV energies. Note that the data slightly favors $\kappa \simeq 0$ values (see §4); the corresponding $j_\nu \propto T^0$ scaling within each halo would be more natural if CRI originate in SNe, rather than in the virial shock. Also note that adiabatic compression of CRI produced at the virial shock and advected with the gas would lead to a radially increasing, $\eta \propto n^{-1/3}$ profile (due the soft equation of state of relativistic particles), which is not observed (see Fig. 2).

We stress that although our model and the model of K09 disagree regarding the origin of CRI, the CRI distribution, the spectral properties of halos, and the role of diffusion, we reach the same conclusions regarding the radio mechanism: emission from secondary CRE in strong magnetic fields. This conclusion is based on *(i)* the tight radio-X-ray correlation in total GH luminosity and the GH bimodality (K09); *(ii)* the tight radio-X-ray correlation in both coincident luminosity and brightness, in both GHs and MHs, despite their different physical properties; *(iii)* the strong magnetic fields inferred from Faraday RMs in MHs and possibly (see §6.1) also in GHs; *(iv)* the tightening of the brightness correlation at small radii, away from merger shocks, radio relics, and their associated turbulence; *(v)* the $j_\nu \propto n^2 T^\kappa$ scaling of the radio emissivity within each halo, where $\kappa \lesssim 1$;

[3] http://www.mwatelescope.org
[4] http://www.lofar.org

(vi) the coincidence between MH edges and CFs, manifest as a sharp radial cutoff in η (*e.g.,* in Perseus); *(vii)* a power-law radial break where $\eta(r \ll r_b) \simeq$ constant and $\eta(r \gg r_b) \propto B^2$ (possibly seen in A2029); *(viii)* the clumpy/filamentary morphology of some halos, where independent evidence for low magnetization is present; *(ix)* the spectral steepening and the correlation between $\langle\alpha\rangle$ and B_0 (this suggests strong magnetization provided that the CRI spectrum is steep, $s \lesssim -2.7$).

Each aspect of our model can be tested in the near future. The association between the presence of halos and strong, $B > B_{cmb}$ magnetic fields can be directly tested by comparing the magnetization levels independently estimated in halo and in non-halo clusters, as illustrated in §6.1. The secondary origin of the halos can be tested if the CRI are detected directly through their π^0 production; for example, such a detection of a CRI component substantially stronger than in Eq. (11) would rule out our model. The SNe origin of the CRI can be tested by examining the correlation between a CRI measure such as η, and an SNe tracer such as the specific SFR, in a sample of halo clusters.

We are deeply grateful to Maxim Markevitch for many fruitful discussions. We thank Ramesh Narayan, Doron Kushnir, Boaz Katz, Eli Waxman, Yuying Zhang, Annalisa Bonafede, Gianfranco Brunetti, Julius Donnert, and Matteo Murgia for useful comments. UK acknowledges support by NASA through Einstein Postdoctoral Fellowship grant number PF8-90059 awarded by the Chandra X-ray Center, which is operated by the Smithsonian Astrophysical Observatory for NASA under contract NAS8-03060. This work was supported in part by NSF grants AST-0907890, AST-08 and NASA LUNAR grant for AL.

REFERENCES

Allen, S. W., Schmidt, R. W., & Fabian, A. C. 2002, MNRAS, 335, 256
Allen, S. W., Schmidt, R. W., Fabian, A. C., & Ebeling, H. 2003, MNRAS, 342, 287
Anderson, M. E., Bregman, J. N., Butler, S. C., & Mullis, C. R. 2009, ApJ, 698, 317
Andersson, K., Peterson, J. R., Madejski, G., & Goobar, A. 2009, ApJ, 696, 1029
Arnaud, K. A. 1996, in Astronomical Society of the Pacific Conference Series, Vol. 101, Astronomical Data Analysis Software and Systems V, ed. G. H. Jacoby & J. Barnes, 17–+
Ascasibar, Y. & Markevitch, M. 2006, ApJ, 650, 102
Augusto, P., Edge, A. C., & Chandler, C. J. 2006, MNRAS, 367, 366
Bacchi, M., Feretti, L., Giovannini, G., & Govoni, F. 2003, A&A, 400, 465
Baldi, A., Ettori, S., Mazzotta, P., Tozzi, P., & Borgani, S. 2007, ApJ, 666, 835
Blattnig, S. R., Swaminathan, S. R., Kruger, A. T., Ngom, M., & Norbury, J. W. 2000, Phys. Rev. D, 62, 094030
Böhringer, H., Voges, W., Huchra, J. P., McLean, B., Giacconi, R., Rosati, P., Burg, R., Mader, J., Schuecker, P., Simiç, D., Komossa, S., Reiprich, T. H., Retzlaff, J., & Trümper, J. 2000, ApJS, 129, 435
Bonafede, A., Feretti, L., Giovannini, G., Govoni, F., Murgia, M., Taylor, G. B., Ebeling, H., Allen, S., Gentile, G., & Pihlström, Y. 2009, A&A, 503, 707
Bonafede, A., Feretti, L., Murgia, M., Govoni, F., Giovannini, G., Dallacasa, D., Dolag, K., & Taylor, G. B. 2010, ArXiv e-prints
Bonamente, M., Joy, M. K., LaRoque, S. J., Carlstrom, J. E., Reese, E. D., & Dawson, K. S. 2006, ApJ, 647, 25
Bregman, J. N., Fabian, A. C., Miller, E. D., & Irwin, J. A. 2006, ApJ, 642, 746
Brunetti, G., Cassano, R., Dolag, K., & Setti, G. 2009, A&A, 507, 661
Brunetti, G. & Lazarian, A. 2007, MNRAS, 378, 245
Brunetti, G., Venturi, T., Dallacasa, D., Cassano, R., Dolag, K., Giacintucci, S., & Setti, G. 2007, ApJ, 670, L5
Carilli, C. L. & Taylor, G. B. 2002, ARA&A, 40, 319
Cassano, R., Brunetti, G., & Setti, G. 2006, MNRAS, 369, 1577
Cassano, R., Gitti, M., & Brunetti, G. 2008, A&A, 486, L31
Cavaliere, A. & Fusco-Femiano, R. 1976, A&A, 49, 137
Chen, Y., Reiprich, T. H., Böhringer, H., Ikebe, Y., & Zhang, Y. 2007, A&A, 466, 805
Clarke, T. E. 2004, Journal of Korean Astronomical Society, 37, 337
Dallacasa, D., Brunetti, G., Giacintucci, S., Cassano, R., Venturi, T., Macario, G., Kassim, N. E., Lane, W., & Setti, G. 2009, ApJ, 699, 1288
David, L. P., Slyz, A., Jones, C., Forman, W., Vrtilek, S. D., & Arnaud, K. A. 1993, ApJ, 412, 479
Dennison, B. 1980, ApJ, 239, L93
Dixon, W. V. D., Davidsen, A. F., & Ferguson, H. C. 1996, AJ, 111, 130
Enßlin, T. A. 2002, A&A, 396, L17
Enßlin, T. A., Lieu, R., & Biermann, P. L. 1999, A&A, 344, 409
Fabian, A. C., Crawford, C. S., Edge, A. C., & Mushotzky, R. F. 1994, MNRAS, 267, 779
Feretti, L., Brunetti, G., Giovannini, G., Kassim, N., Orrú, E., & Setti, G. 2004a, Journal of Korean Astronomical Society, 37, 315
Feretti, L., Fusco-Femiano, R., Giovannini, G., & Govoni, F. 2001, A&A, 373, 106
Feretti, L. & Giovannini, G. 2008, in Lecture Notes in Physics, Berlin Springer Verlag, Vol. 740, A Pan-Chromatic View of Clusters of Galaxies and the Large-Scale Structure, ed. M. Plionis, O. López-Cruz, & D. Hughes, 143–+
Feretti, L., Giovannini, G., & Bohringer, H. 1997, New Astronomy, 2, 501
Feretti, L., Orrù, E., Brunetti, G., Giovannini, G., Kassim, N., & Setti, G. 2004b, A&A, 423, 111
Ferrari, C., Govoni, F., Schindler, S., Bykov, A. M., & Rephaeli, Y. 2008, Space Science Reviews, 134, 93
Fukazawa, Y., Makishima, K., & Ohashi, T. 2004, PASJ, 56, 965
Giacintucci, S., Venturi, T., Brunetti, G., Bardelli, S., Dallacasa, D., Ettori, S., Finoguenov, A., Rao, A. P., & Zucca, E. 2005, A&A, 440, 867
Giacintucci, S., Venturi, T., Brunetti, G., Dallacasa, D., Mazzotta, P., Cassano, R., Bardelli, S., & Zucca, E. 2009, A&A, 505, 45
Ginzburg, V. L. & Syrovatsky, S. I. 1961, Progress of Theoretical Physics Supplement, 20, 1
Giovannini, G., Bonafede, A., Feretti, L., Govoni, F., Murgia, M., Ferrari, F., & Monti, G. 2009, A&A, 507, 1257
Giovannini, G., Feretti, L., Bacchi, M., & Govoni, F. 2003, in Astronomical Society of the Pacific Conference Series, Vol. 301, Astronomical Society of the Pacific Conference Series, ed. S. Bowyer & C.-Y. Hwang, 483–+
Giovannini, G., Feretti, L., Venturi, T., Kim, K., & Kronberg, P. P. 1993, ApJ, 406, 399
Gitti, M., Brunetti, G., Feretti, L., & Setti, G. 2004, A&A, 417, 1
Gitti, M., Brunetti, G., & Setti, G. 2002, A&A, 386, 456
Govoni, F., Enßlin, T. A., Feretti, L., & Giovannini, G. 2001a, A&A, 369, 441
Govoni, F., Feretti, L., Giovannini, G., Böhringer, H., Reiprich, T. H., & Murgia, M. 2001b, A&A, 376, 803
Govoni, F., Markevitch, M., Vikhlinin, A., VanSpeybroeck, L., Feretti, L., & Giovannini, G. 2004, ApJ, 605, 695
Govoni, F., Murgia, M., Feretti, L., Giovannini, G., Dallacasa, D., & Taylor, G. B. 2005, A&A, 430, L5
Govoni, F., Murgia, M., Markevitch, M., Feretti, L., Giovannini, G., Taylor, G. B., & Carretti, E. 2009, A&A, 499, 371
Guidetti, D., Murgia, M., Govoni, F., Parma, P., Gregorini, L., de Ruiter, H. R., Cameron, R. A., & Fanti, R. 2008, A&A, 483, 699

Harris, D. E., Kapahi, V. K., & Ekers, R. D. 1980, A&AS, 39, 215
Kaastra, J. S. 1992, An X-Ray Spectral Code for Optically Thin Plasmas, Internal SRON-Leiden Report, updated version 2.0
Kamae, T., Karlsson, N., Mizuno, T., Abe, T., & Koi, T. 2006, ApJ, 647, 692
Kempner, J. C. & Sarazin, C. L. 2001, ApJ, 548, 639
Keshet, U., Markevitch, M., Birnboim, Y., & Loeb, A. 2009, ArXiv e-prints
Keshet, U., Waxman, E., Loeb, A., Springel, V., & Hernquist, L. 2003, ApJ, 585, 128
Kushnir, D., Katz, B., & Waxman, E. 2009, Journal of Cosmology and Astro-Particle Physics, 9, 24 (K09)
Kushnir, D. & Waxman, E. 2010, Journal of Cosmology and Astro-Particle Physics, 2, 25
Lewis, A. D., Buote, D. A., & Stocke, J. T. 2003, ApJ, 586, 135
Liedahl, D. A., Osterheld, A. L., & Goldstein, W. H. 1995, ApJ, 438, L115
López-Cruz, O., Barkhouse, W. A., & Yee, H. K. C. 2004, ApJ, 614, 679
Macario, G., Venturi, T., Brunetti, G., Dallacasa, D., Giacintucci, S., Cassano, R., Bardelli, S., & Athreya, R. 2010, ArXiv e-prints
Markevitch, M. 1998, ApJ, 504, 27
Markevitch, M. & Vikhlinin, A. 2001, ApJ, 563, 95
—. 2007, Phys. Rep., 443, 1
Matsumoto, H., Pierre, M., Tsuru, T. G., & Davis, D. S. 2001, A&A, 374, 28
Matsumoto, H., Tsuru, T. G., Fukazawa, Y., Hattori, M., & Davis, D. S. 2000, PASJ, 52, 153
Mazzotta, P. & Giacintucci, S. 2008, ApJ, 675, L9
Mewe, R., Gronenschild, E. H. B. M., & van den Oord, G. H. J. 1985, A&AS, 62, 197
Mewe, R., Lemen, J. R., & van den Oord, G. H. J. 1986, A&AS, 65, 511
Morandi, A., Ettori, S., & Moscardini, L. 2007, MNRAS, 379, 518
Murgia, M., Govoni, F., Feretti, L., Giovannini, G., Dallacasa, D., Fanti, R., Taylor, G. B., & Dolag, K. 2004, A&A, 424, 429
Murgia, M., Govoni, F., Markevitch, M., Feretti, L., Giovannini, G., Taylor, G. B., & Carretti, E. 2009, A&A, 499, 679 (M09)
Norbury, J. W. 2009, Nuclear Instruments and Methods in Physics Research B, 267, 1209
Orrú, E., Murgia, M., Feretti, L., Govoni, F., Brunetti, G., Giovannini, G., Girardi, M., & Setti, G. 2007, A&A, 467, 943
Peterson, J. R. & Fabian, A. C. 2006, Phys. Rep., 427, 1
Petrosian, V. & Bykov, A. M. 2008, Space Science Reviews, 134, 207
Rafferty, D. A., McNamara, B. R., & Nulsen, P. E. J. 2008, ApJ, 687, 899
Reiprich, T. H. & Böhringer, H. 2002, ApJ, 567, 716
Rephaeli, Y., Nevalainen, J., Ohashi, T., & Bykov, A. M. 2008, Space Science Reviews, 134, 71
Roland, J., Sol, H., Pauliny-Toth, I., & Witzel, A. 1981, A&A, 100, 7
Rudnick, L. & Lemmerman, J. A. 2009, ApJ, 697, 1341
Sanderson, A. J. R., O'Sullivan, E., & Ponman, T. J. 2009, MNRAS, 395, 764
Santos, J. S., Rosati, P., Tozzi, P., Böhringer, H., Ettori, S., & Bignamini, A. 2008, A&A, 483, 35
Schilizzi, R. T., Alexander, P., Cordes, J. M., Dewdney, P. E., Ekers, R. D., Faulkner, A. J., Gaensler, B. M., Hall, P. J., Jonas, J. L., & Kellermann, K. I. 2007, Preliminary Specifications for the Square Kilometre Array, Kilometre Array collaboration document (2007), http://www.skatelescope.org/pages/page_astronom.htm
Slee, O. B. & Siegman, B. C. 1983, Proceedings of the Astronomical Society of Australia, 5, 114
Snowden, S. L., Mushotzky, R. F., Kuntz, K. D., & Davis, D. S. 2008, A&A, 478, 615
Taylor, G. B., Fabian, A. C., & Allen, S. W. 2002, MNRAS, 334, 769
Valtchanov, I., Murphy, T., Pierre, M., Hunstead, R., & Lémonon, L. 2002, A&A, 392, 795
van Weeren, R. J., Röttgering, H. J. A., Brüggen, M., & Cohen, A. 2009, A&A, 508, 75
Vikhlinin, A., Kravtsov, A., Forman, W., Jones, C., Markevitch, M., Murray, S. S., & Van Speybroeck, L. 2006, ApJ, 640, 691
Vogt, C. & Enßlin, T. A. 2005, A&A, 434, 67
Völk, H. J., Aharonian, F. A., & Breitschwerdt, D. 1996, Space Science Reviews, 75, 279
White, D. A. 2000, MNRAS, 312, 663
Worrall, D. M. & Birkinshaw, M. 2003, MNRAS, 340, 1261
Zhang, Y., Finoguenov, A., Böhringer, H., Kneib, J., Smith, G. P., Kneissl, R., Okabe, N., & Dahle, H. 2008, A&A, 482, 451